Performance of Isolated Footing with Several Corrosion Levels under Axial Loading

Ahmed Youssef [1*] , Mahmoud Hegazy [1, 2] , Hatem Mostafa [1]

[1] Department of Structure Engineering, Cairo University, Giza, 12613, Egypt.

[2] Department of Civil Engineering, Institute of Aviation and Engineering Technology, Giza, Egypt.

Abstract

This research aims to illustrate the corrosion process and its effect on the deterioration of reinforced concrete (RC) isolated footings using a small-scale model (1/8) and present the results of a prototype-scale study using a numerical model with different concrete depths and corrosion levels under axial load. The experimental program consisted of testing five small-scale (1/8) model RC isolated footings under axial loading after subjecting them to accelerated corrosion tests with a constant current. The main variable in the small-scale sample test was the corrosion level. This study presents an experimental approach, using the constant current method and the finite element method (FEM) with the ABAQUS package, to examine its effect on the axial load behavior under different corrosion ratios, which were 0%, 4.21%, 9.11%, 24.56%, and 30.67%. On the prototype scale, the variables were the corrosion level and the RC depths of 300 mm, 400 mm, and 500 mm. The results indicated that the average deviation in ultimate load between the experimental and FEM outcomes for the small-scale was below 5.6%, while the average deflection deviation was 6.8%. Also, the study found that an increase in the depth of the RC footing and corrosion ratio led to a more pronounced impact of the cracking pattern in the concrete and corroded bars, as well as a greater difference in the failure load. The experimental results suggest that the proposed numerical model is accurate and effective. These findings have important implications for the evaluation of isolated footings affected by corrosion damage using FEM, and can help inform decisions related to their design and maintenance. The failure loads of non-corroded footings with different depths were compared with the ECP-203 provisions of the 2018 Egyptian Code, and how corrosion ratios can be simulated by numerical models. The percentage variation between the design loads by code and the numerical loads by ABAQUS for controlled footings with thicknesses of 300, 400, and 500 mm was found to be 73%, 80%, and 78%, respectively. Using the derived relationship, the equivalent corrosion ratio percentages were 23.8%, 20.2%, and 32%, respectively.

Keywords: Acceleration Corrosion-Constant Current; Axial Loading; Isolated Footing; Finite Element Modeling; Small Scale Modeling.

1. Introduction

The durability of RC buildings that are exposed to chloride can be significantly reduced due to the corrosion of steel bars [1–3]. The load-bearing capacity of steel bars is diminished, and the bond between concrete and corroded steel is weakened when the cross-sectional area of steel bars decreases as a result of corrosion. Consequently, the confinement offered by transverse reinforcement is diminished, and the steel's mechanical properties are altered [4]. Many RC elements, such as footings, are situated in salt-prone and coastal areas; however, the behavior of RC footings under axial loading with varying corrosion levels has not been as thoroughly researched as other RC components like columns, slabs, and beams. This study was to investigate the performance of the isolated footing exposed to different degrees of corrosion.

There have been numerous studies on corrosion in various RC elements. Zaghian et al. (2023) [5] discovered that reinforcing steel corrosion is the main cause of concrete degradation in North American infrastructure, with piers being particularly susceptible. Using de-icing salts in coastal regions exacerbates this vulnerability. Corrosion increases nonlinearity and affects the failure of slender, eccentrically loaded columns. The study employed a comprehensive model of corrosion damage and a step-by-step corrosion scenario to investigate how the capacity, stiffness, and ductility of bridge columns are impacted by corrosion under the influence of off-center loads. To ensure accuracy, the model was verified by comparing it to data from prior experiments. Also, El-Joukhadar et al. (2023) [6] established standards for evaluating the impact of corrosion damage on column seismic resistance. Current guidelines do not consider bar corrosion, which affects mechanical properties and seismic performance. The suggested changes to the nonlinear assessment involve adjusting reduction factors for stress-strain characteristics, stiffness, strength, and deformation capacity. These factors will be calibrated using a database of corroded columns obtained from experiments. Advanced finite element analysis considers the mass loss effect on material properties. It may be complicated to incorporate corrosion effects into evaluations, but it is necessary for accurate results.

Wang et al. (2023) [7] Experiments were carried out by utilizing accelerated corrosion techniques and conducting tests that generated shearing forces between surfaces. The aim of the investigations was to explain how corrosion affects the strength of the connection between steel foundations and the soil in their vicinity. According to the findings, there was a positive correlation between the level of corrosion and both interfacial cohesiveness and the friction coefficient. Finite element simulations further emphasized the importance of considering changes in the interfacial shearing property caused by corrosion. A similar study to Wang et al. (2022) [8] indicates that steel foundations in ocean engineering are at risk of corrosion, which could be a safety hazard. Despite the significance of the surface roughness properties of corroded steel foundations in submarine soil, which can impact soil-structure interaction and bearing capacity, there has been insufficient research conducted on this topic. To address gaps in previous research, the study also developed a stochastic model to simulate the surface properties of corroded steel. These results and models can be beneficial for analyzing the interaction between soil and steel foundations and the bearing capacity of engineering structures in the ocean while taking corrosion into account.

Li et al. (2023) [9] found that corrosion of reinforcing bars in RC members can significantly affect their seismic performance and collapse mechanism. The researcher carried out tests on four specimens with varying rates of corrosion to examine the cyclic loading effect on RC shear walls exposed to corrosion. RC shear walls experienced an adverse impact on their seismic performance, particularly in cases where corrosion was severe. The researchers suggested both analytical and finite element models incorporate the effects of corrosion on the shear strength and deterioration of shear walls. Meanwhile, Han et al. (2023) [10] used capacitance-based rebar corrosion detection, numerical simulations, and acceleration tests to study the corrosion effect on RC structures. By placing capacitance sensors in different electrode positions, the authors established a formula for non-uniform corrosion and evaluated RC sample compactness. On the other hand, Zheng et al. (2022) [11] examined chloride effects on the induced corrosion of reinforcement bars on the seismic performance of squat RC walls. They subjected eight specimens to accelerated corrosion and pseudo-static tests and found that the specimens' bearing, deformation, and energy dissipation capacities decreased as the corrosion levels increased. The authors also developed a new equation for the corroded squat wall skeleton curve's distinctive point characteristics.

Zhao et al. (2021) [12] Cyclic load experiments have been tested on four scaled Samples of bridge piers exposed to varying amounts of accelerated corrosion process in the anticipated splash and tidal zones. They observed a reduction in ductility, load-bearing capacity, and cumulative energy consumption as corrosion levels increased. Finally, Hu et al. (2021) [13] indicate that the impact of stochastic pitting on the functionality of ship hull plates was explored by employing a numerical simulation technique and a Python script. Their approach was validated by conducting a pitting test and subsequently utilized to evaluate the impact of different stochastic pitting patterns on the ultimate strength of stiffened plates, and the tensile characteristics of unstiffened plates.

Altoubat et al. (2016) [14] investigated steel corrosion in RC columns. They conducted axial loading experiments on six small-scale, corroded RC columns at various levels. Kasetni et al. (2016) [15] presented a FEM that simulates the nonlinear performance of a corroded RC fiber beam-column member. Mohammed et al. (2020) [16] discussed the behavior of corroded RC elements using numerical analysis. Khalid (2018) [17] conducted a numerical analysis using the axial ABAQUS-3D model to simulate deteriorated columns and found that the FEM findings were compatible with the experimental outcomes. Fang et al. (2021) [18] studied the flexural behavior of corroded RC slabs.

This study illustrates the performance of corroded (RC) footings under the axial loading experimental program and numerical models. Corrosion levels were tested at ratios of 0%, 4.21%, 9.11%, 24.56%, and 30.67%, measured by the loss of steel bar area. The effect of corrosion on the bond strength between rusted steel and concrete was demonstrated by utilizing the concrete-damaged plasticity model (CDP) and the ABAQUS package, with an expansion model being employed.

In addition to the experimental results, this research shows numerical models for prototype-scale RC footings with varying depths of concrete (300 mm, 400 mm, and 500 mm) and different levels of corrosion. It's used to illustrate the effect of concrete depth on axial load performance under different corrosion levels. Based on the results, the study proposes that load-bearing capacity decreases with increasing corrosion levels and suggests that isolated corrosion cracks in the footing may occur.

2. Experimental Program Properties

2.1. Specimen Dimensions

This study used five small-scale 1/8-isolated reinforced concrete (RC) specimens, as shown in Figure 1, with dimensions of 250×250 mm, a thickness of 40 mm, and 5 mm as a concrete cover. The column was made from a 40 x 40-mm steel tube with a thickness of 2 mm and a height of 140 mm filled with RC concrete, scaled down from a prototype-scale footing with dimensions of 2000×2000 mm, 300 mm thickness, and a 300×300 mm column. According to the Egyptian Code [19], the smallest allowable depth for an RC footing is determined by the largest value between 300 mm or a dimension that is less than the column dimension, which corresponds to the most vulnerable scenario. The specimens had a compressive strength f_{cu} of 40 N/mm^2 and 7 bars with a diameter of 2 mm in each direction. The yield strength f_y and tensile strength fu of the steel bars used in the small-scale specimens were 850 N/mm^2 and 978 N/mm^2, respectively. The corrosion level ratio was the main variable, and the specimens had corrosion ratios of 0%, 4.21%, 9.11%, 24.56%, and 30.67%. The specimens were labeled as S_p x, where x represents the rebar corrosion loss ratio%, and S_p 4.21 represents a reinforced concrete footing with a corrosion bar loss ratio of 4.21%.
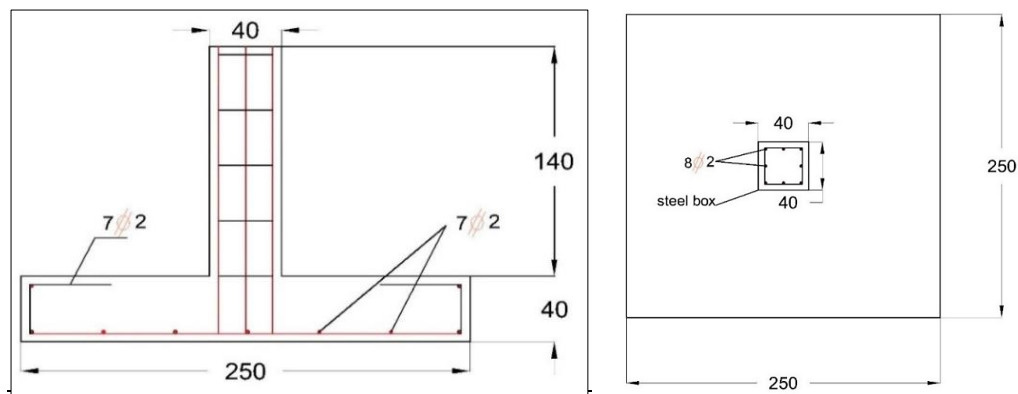

Figure 1. Dimension of test small-scale specimen (unit: mm)

2.2. Material Properties

A cement mortar consisting of cement and sand was used, with a proportion of cement: water: sand = 1:0.42:1.25 by weight. The compressive properties of the concrete were assessed by conducting tests on three standard cubes (measuring 70×70×70 mm) after 28 days, which indicated a compressive strength of 40 N/mm^2. Figure 2 depicts the wooden model, a steel bar, and a sample of footing after casting. Table 1 displays the physical characteristics of the 2 mm diameter steel bar, and the relationship between stress and strain is shown in Figure 3.
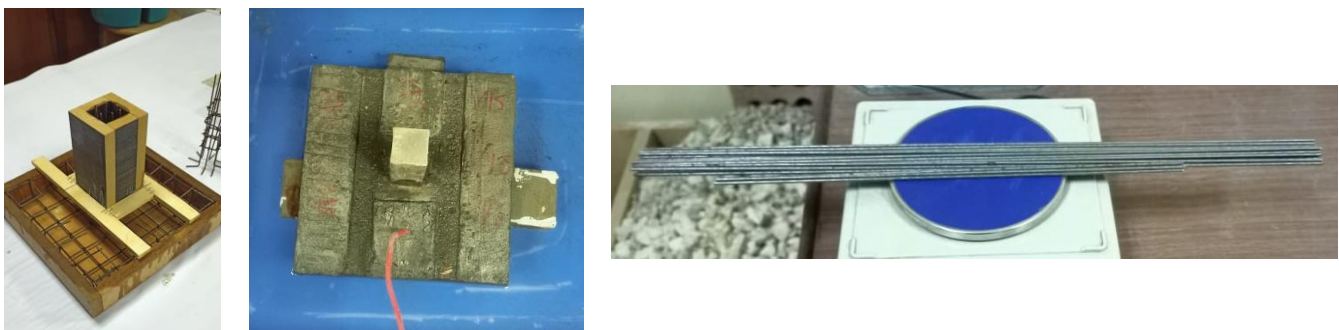

Figure 2. The wooden model, steel bar, and a sample of footing after casting

Table 1. The mechanical characteristics of the reinforcement steel bars

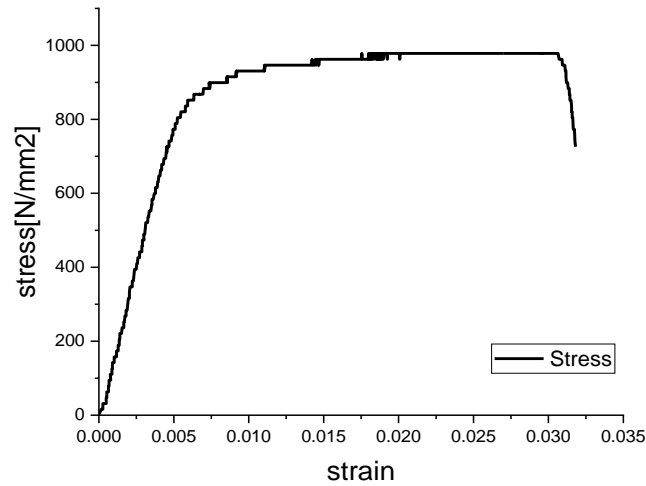| Bar diameter (mm)	Weight (gm)	Length (mm)	Calculated area (mm²)	Yield proof load (kN)	Ultimate proof load (kN)	Yield-proof stress (N/mm²)	Ultimate proof stress (N/mm²)	Elongation (%)
2	7.9	275	3.14	2.571	3.071	850	978	1.46

Figure 3. The relationship between stress and strain for the used steel

Properties of the sandy soil: As shown in Figure 4, a circular steel tank (560 mm in diameter and 280 mm in height) was filled with medium-density sand to simulate real soil. The sand was compacted in three equal layers of 280/3 mm thickness with a steel block weight of 3.650 kg.

Figure 4. Tested soil tank

The soil was tested in a soil laboratory (Sieve analysis and shear box test) to determine its properties and found as:

- Fineness modulus was 3.55;
- Coefficient Of Curvature Cc = 0.85;
- Dry density ($\curlyvee_{dry}$ = 14.6 kN/m³);
- Friction Angle (Ø) = 35.0°;
- Uniformity Coefficient Cu = 3.28;

Figures 5 to 7 show the sieve analysis chart, the relation between shear strength and shear distance, and the relation between shear strength and normal stress, respectively.
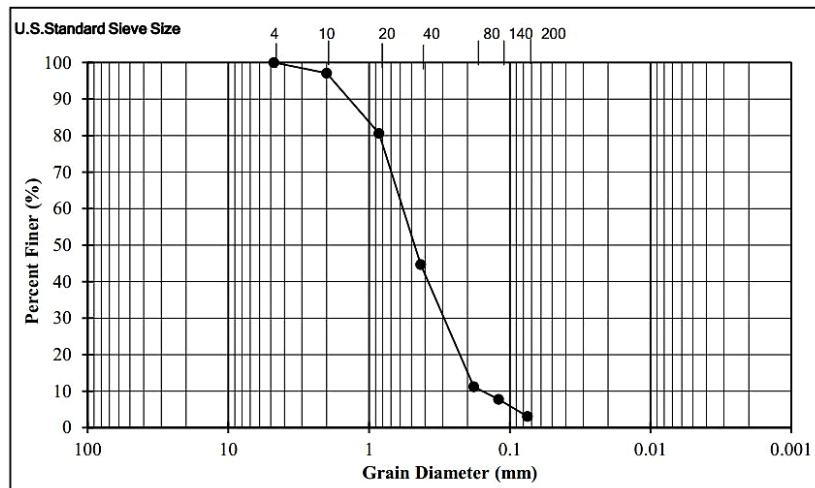

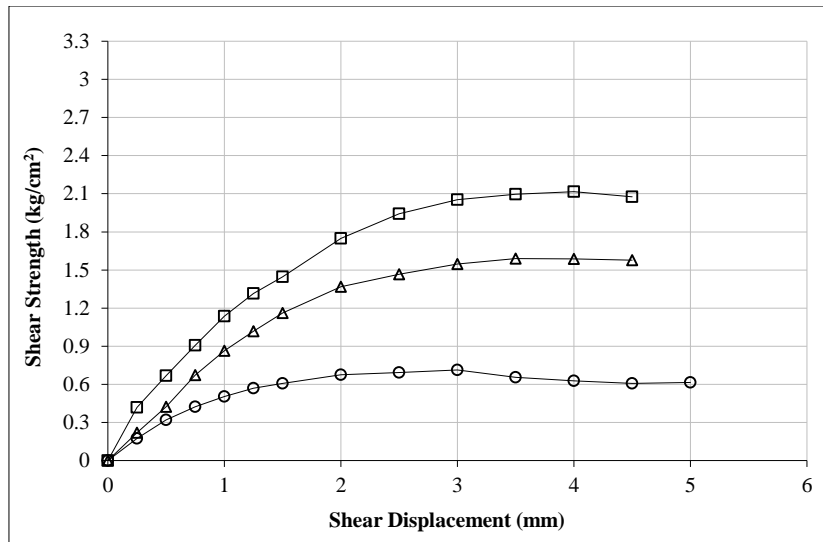**Figure 5. Sieve analysis chart of the used sand soil**

Figure 6. The relationship between shear strength and shear distance of the used sand soil
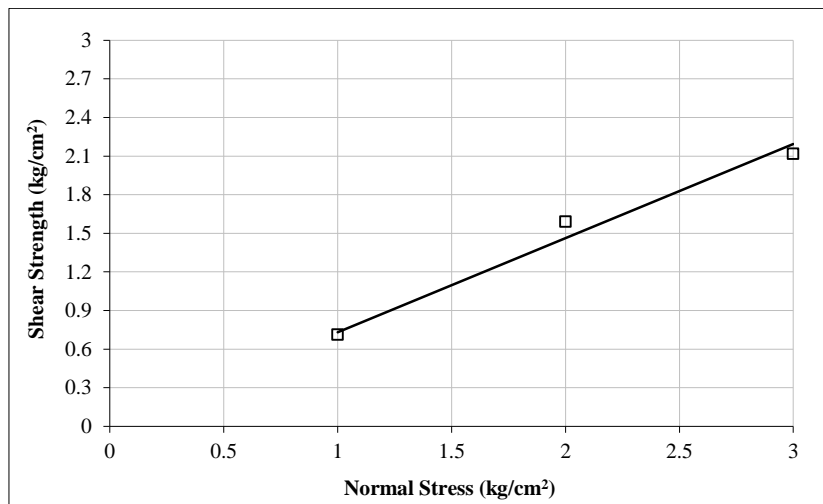

Figure 7. Shear strength and normal stress relationship of the used sand soil

2.3. The Corrosion Processes

To assess the extent of corrosion in small-scale models, a constant current approach was employed as an accelerated corrosion method. The samples were submerged in a 5% NaCl solution, and a constant current of known value was supplied by the anode (the reinforcing mesh of each specimen) and the cathode (a steel plate immersed in the tank) [20]. The mass losses in the steel bar were used to estimate the degree of corrosion using Faraday's law [21]. This approach provides a reliable indication of the expected corrosion level and enables an assessment of the potential long-term effects on the structure.

$$T = (3446.429 \times \frac{1}{3600} \times \frac{Mloss}{Icorr} \ [hr.] \tag{1}$$

where (T) is the time when corrosion occurs by an hour [hr.], (I_{corr}) is current by Ampere [A], and (M_{loss}) is the losses in the mass by gram [gm].

By representing the actual corrosion level (X) as the variation between the initial weight and the final weight relative to the weight before corrosion,

$$X = \frac{(MI - MF)}{MI} \times 100 \ \% \tag{2}$$

where M_I is initial weight of steel bar and M_F is Final weight of steel bar.

The calculated M_{loss} ratios of rusted bars corresponding to the corrosion levels are shown in Table 2. They were calculated by weighing the steel bars after the loading test and breaking the models, and cleaning the outer surface of the steel bars from rust. Figure 8 shows the power supply used in this process.

Table 2. Characteristics of the specimens

Specimen	M_I (gm)	I_{corr} (A)	T (hr)	M_F (gm)	Corrosion loss ratio X (%)
Sp $_0$	201.02	-	-	201.02	0
Sp $_{4.21}$	201.49	0.1	192.69	193	4.21
Sp $_{9.11}$	198.05	0.1	378.79	180	9.11
Sp $_{24.56}$	201.49	0.1	578.05	152	24.56
Sp $_{30.67}$	200.50	0.1	766.96	139	30.67

Figure 8. Power supply

2.4. Test Setup

To simulate real soil conditions, all footing specimens were situated in the center of a circular steel tank filled with medium-density sand, as shown in Figure 9. The samples were exposed to a concentrated force using a vertical load cell to measure the load applied. In order to track any deformation or bending of the column under load, two displacement gauges were used to measure the vertical displacement from the column head and the footing top surface at the edge of the center axis of the footing. By comparing the displacement measurements at different points, the researchers could study how the load was distributed across the system and how the footing influenced the overall structural behavior. The vertical displacement measurement at the top of the column provided valuable information on the behavior and capacity of the column and its ability to bear the load without breaking or undergoing excessive deformation.

Figure 9. Loading frame

3. Numerical Simulation

The evaluation of corrosion damage was carried out in this study using the ABAQUS software [22], employing the concrete damage plasticity (CDP) model. The uniaxial stress approach was used to define the concrete's properties, and the parameters and their effect under compound stress are demonstrated in Table 3. The mechanical characteristics of concrete, steel bar, and sand were defined and presented in Table 4.

Table 3. The concrete damage plasticity (CDP) models parameter [23]

Parameter	Dilation angle	Eccentricity angle	f_b/f_c	K	Viscosity parameter
Value	40	0.1	1.16	0.667	0

Table 4. Properties of concrete, steel bar, and sand

| Material properties	Modulus of elasticity [N/mm^2]	Poisson's ratio
Concrete	33345.76	0.2
Steel bar	2100000	0.3
Corrosion bars @ 4.21%-9.11 %	120000 [24]	0.45 (assumed)
Corrosion bars @ 24.56 %	60000	0.45 (assumed)
Corrosion bars @ 30.67 %	50000	0.45 (assumed)
Medium dense sand	15	0.35

ABAQUS software was employed to simulate the non-linear behavior of concrete under the influence of corrosion in reinforced steel bars. Specific elements such as the "solid element," representing the concrete, and the "wire element," representing the steel reinforcing bars. To describe the non-linear behavior of concrete affected by corrosion in reinforced steel bars, the "damaged plasticity concrete (CDP)" model was employed, while the "plastic/isotropic" model was used to model the reinforcement steel. The study examined the impact of corrosion on three factors: a decrease in the bond strength between steel reinforcement and concrete, a decrease in the cross-sectional area of reinforcing bars, and a modification in steel characteristics during the corrosion process. The "embedded region" constraint in ABAQUS is used for simulating the slippage between concrete and the steel bars, assuming strain compatibility or a full connection between the two materials. Nevertheless, this technique may not accurately replicate the significant reduction in the connection between the steel reinforcement and concrete. Therefore, a new approach for simulating this interaction should be developed. Corrosion causes concrete cracking when the corroded steel volume increases relative to the initial volume of the steel bars, leading to increased pressure and potential surface spreading. The cross-section of the reinforcing steel decreased due to corrosion, with a corrosion expansion coefficient (v) of 3 selected for this study [22]. As shown in Figure 10, the load was represented as a vertical displacement line from the top surface of the column.
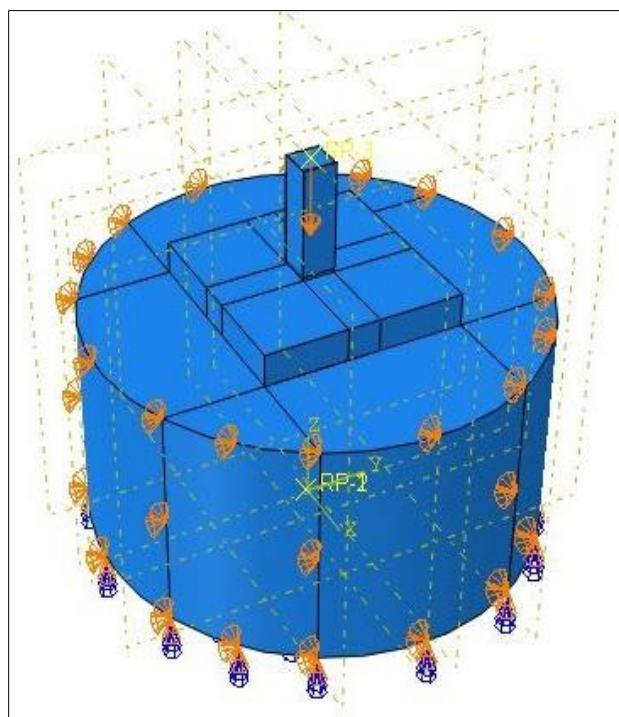
**Figure 10. The displacement line applied to the column**

4. Experimental and Numerical Results and Discussion of Small-Scale Model

4.1. Corrosion and Cracking Pattern Distribution

Experimental and numerical results in Figures 11 and 12 were used to analyze and compare crack distribution due to failure loads and after the corrosion process. The control specimen, Sp 0, showed a flexure crack in the middle of the footing in each direction at the bottom due to its tensile strength. However, the first crack in corroded specimens, Sp 4.21, Sp 9.11, Sp 24.56, and Sp 30.67, appeared due to flexure load and then gradually increased diagonally, leading to punching failure. Through a comparison of the crack distribution between the control and corroded specimens, the study identified the corrosion impact on the strength of footings. These results can offer important insights for the design and maintenance of RC structures that are vulnerable to corrosion.
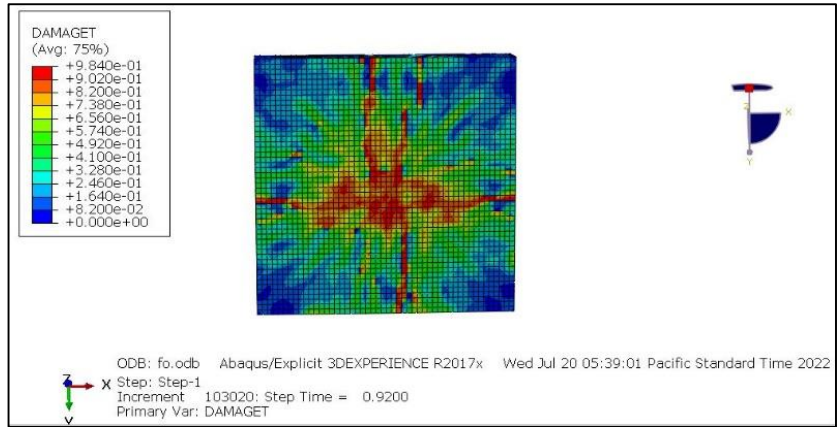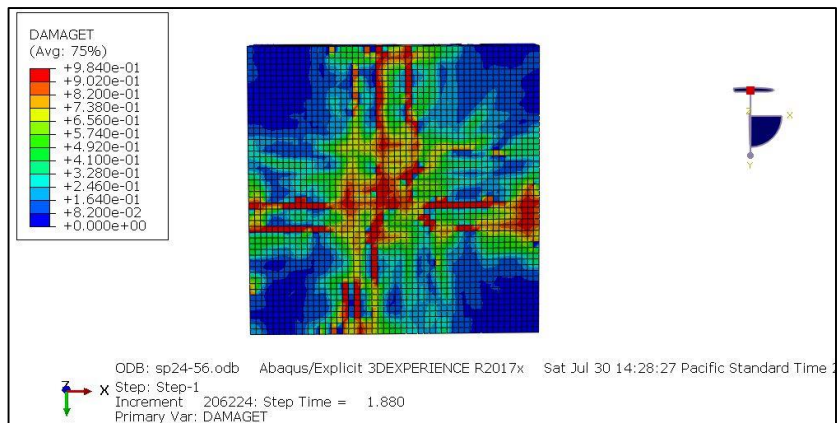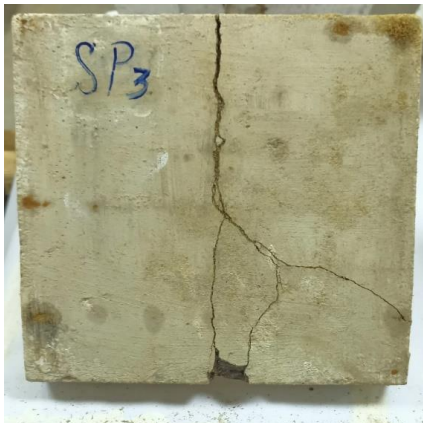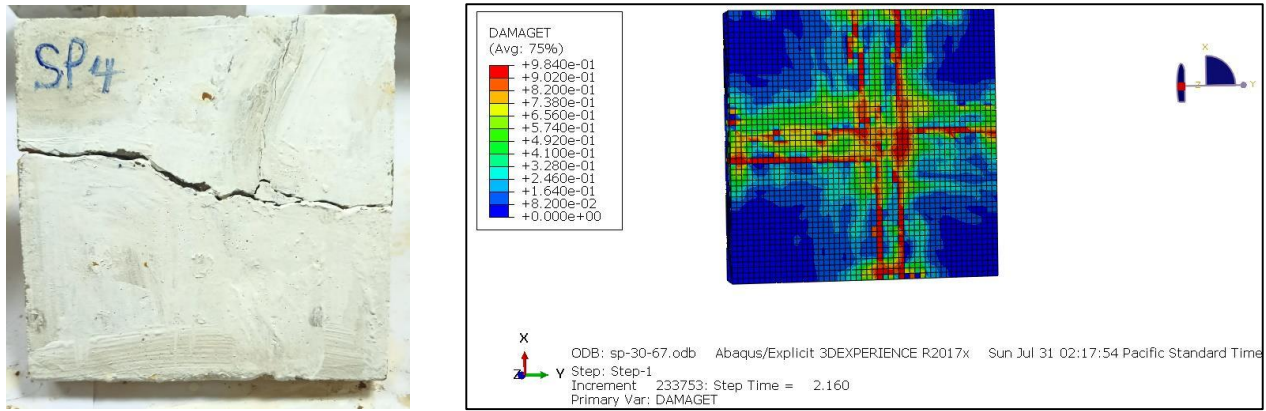
(a) Sp 0
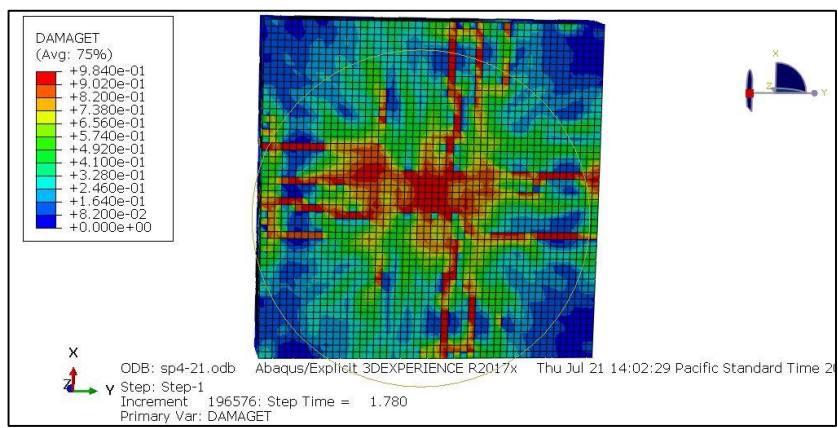
(b) Sp 4.21
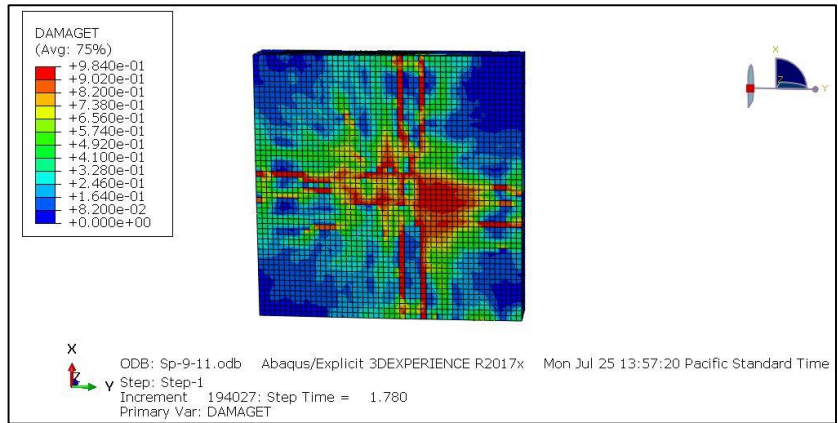
(c) Sp 9.11

(d) Sp 24.56

(e) Sp 30.67

Figure 11. Distribution of corrosion-induced crack: a) Sp 0; b) Sp 4.21; c) Sp 9.11; d) Sp 24.56; e) Sp 30.67

(a) Sp 4.21

(b) Sp 9.11

(c) Sp 24.56

(d) Sp 30.67

Figure 12. Distribution of corrosion due to the accelerated corrosion process. a) Sp 4.21, b) Sp 9.11, c) Sp 24.56, d) Sp 30.67

4.2. Load – Deflection Curve

Various small concrete footing models with various degrees of corrosion were examined under axial loading. The load-displacement graphs showed that the non-corroded control model (Sp 0) exhibited higher stiffness and capacity to withstand loads compared to the corroded models. Specifically, the control model failed at the highest load of 42.6 kN. In contrast, the corroded models failed at lower loads of 35.4 kN, 34.3 kN, 26.9 kN, and 22.9 kN for Sp 4.21, Sp 9.11, Sp 24.56, and Sp 30.67, respectively. Overall, the results demonstrated that corrosion reduced the load-bearing capacity and stiffness of the concrete footings (Figure 13).
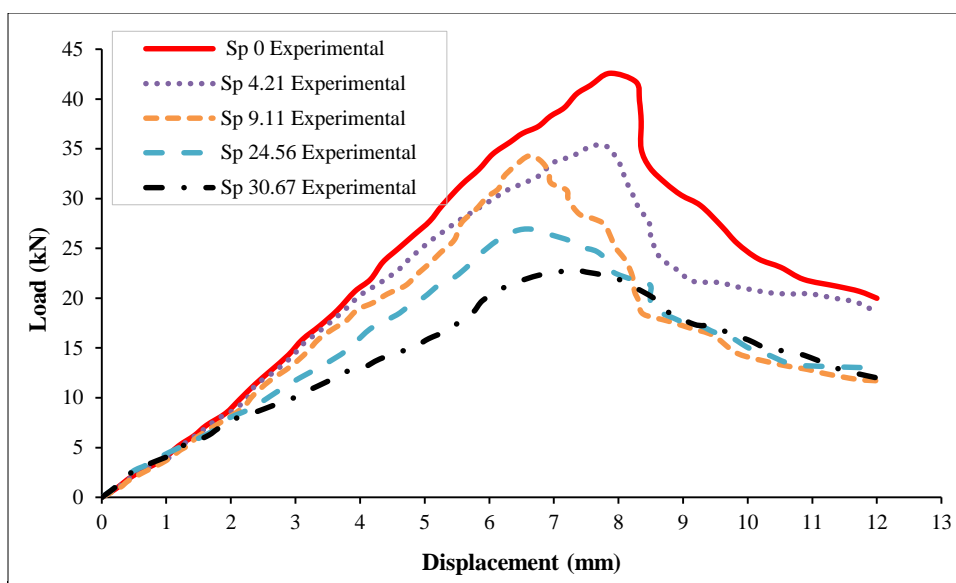
Figure 13. Experimental Envelope curve of the specimens

In Figure 14, the relationship between the load bearing capacity and displacement of the corroded footing subjected to axial load is depicted, along with the corresponding numerical results. The findings reveal a significant deterioration in both stiffness and failure load of the corroded footing when compared to the control footing. Specifically, the control footing (Sp 0) had a failure load of 40.2 kN, while the footings (Sp 4.21, Sp 9.11, Sp 24.56, and Sp 30.67) had failure loads of 33.6 kN, 32.9 kN, 28.6 kN, and 24.7 kN, respectively.
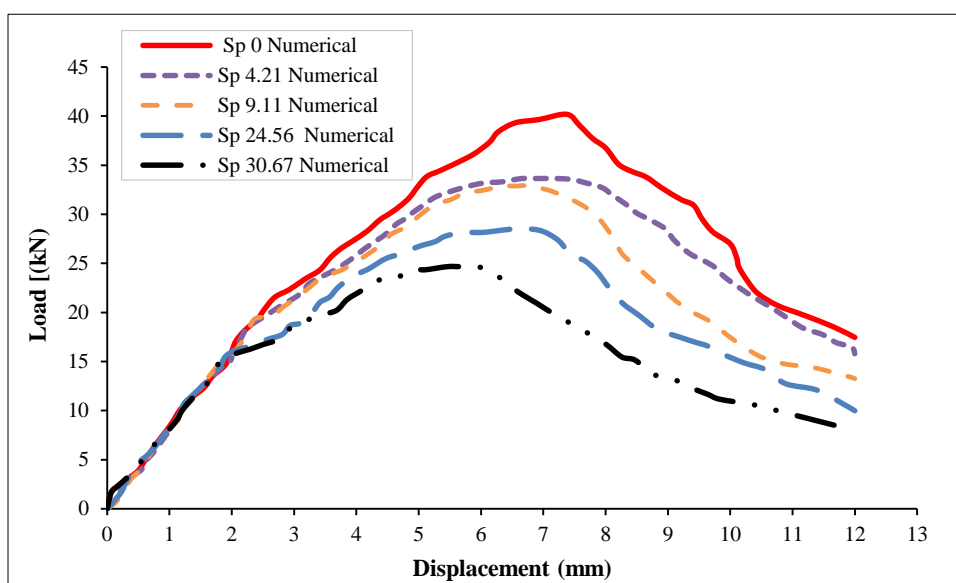

Figure 14. Numerical Envelope curve of the specimens

Figures 15 and 16 illustrate the correlation between failure load and displacement for corroded footings that are subjected to axial compression, using both experimental and numerical data. Although there is a slight difference at the beginning of the load-displacement curve, the behavior is mostly the same. The curves indicate that corroded footings have lower failure loads at larger displacements compared to non-corroded ones. While corrosion degradation reduces the strength capacity of the footings, the overall load-displacement relationship remains largely the same, with the curves diverging at higher deformations. Table 5 provides data on failure loads, displacements, and numerical-to-experimental result ratios, indicating a considerable degree of concurrence between the experimental data and the finite element model. The average difference in ultimate load and deflection at failure between the experimental and finite element model values for small-scale specimens was less than 5.6% and 6.8%, respectively. In conclusion, the analysis by FEM was able to accurately predict the strength and deformation response of corroded footings, with differences of less than 6% compared to experimental data. The model is reliable and can be used to further investigate the behavior of corroded concrete structures. Additionally, Figure 17 shows the correlation between the percentage of corrosion and the decrease in load capacity relative to non-corroded footings in a different way.
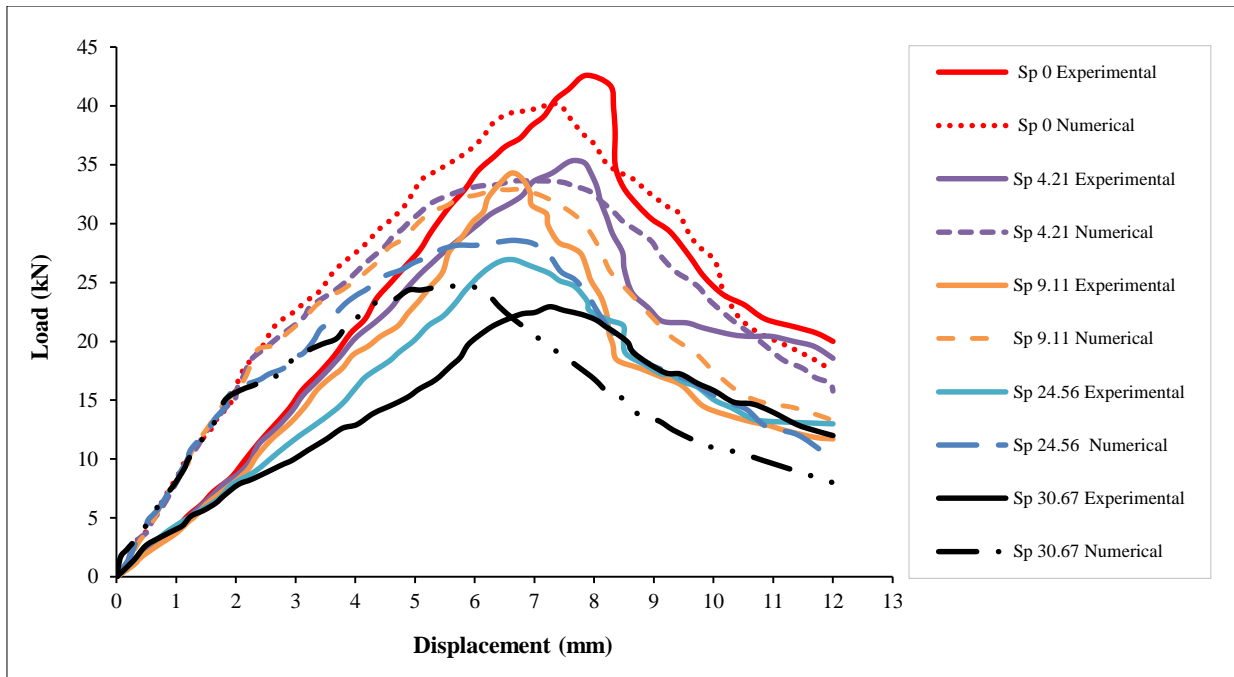
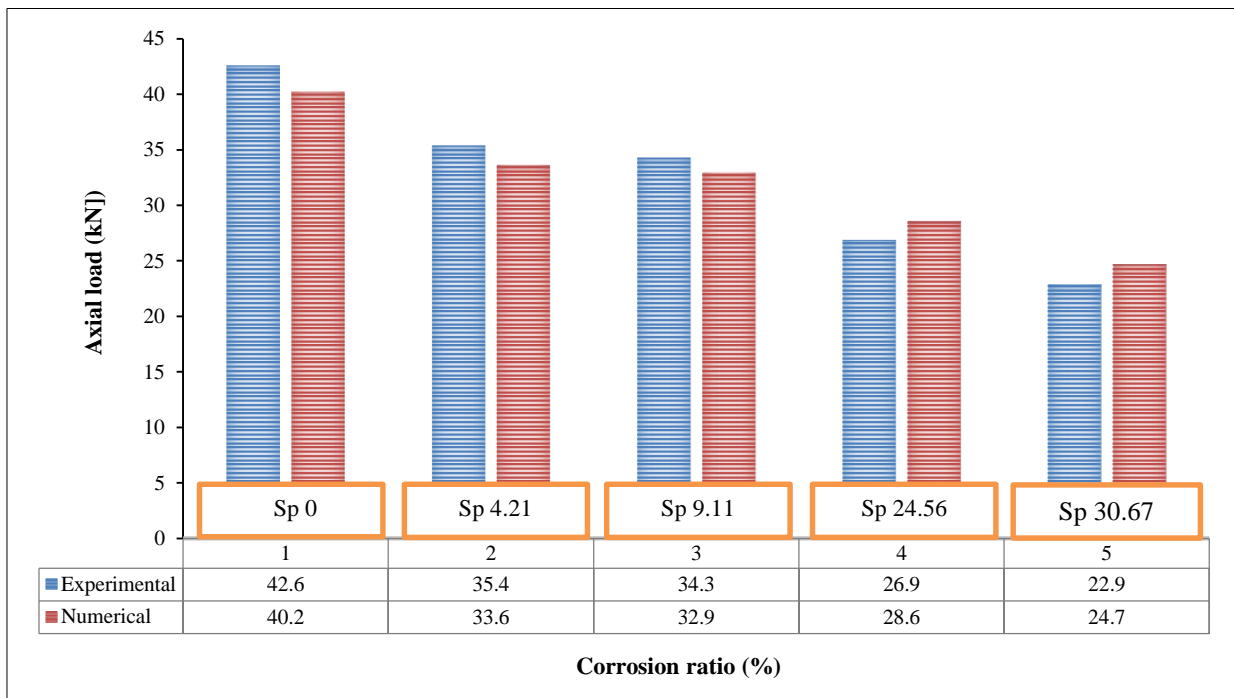**Figure 15. Experimental and Numerical Envelope curve of the specimens**

Figure 16. Comparison of load capacity

Table 5. Experimental and Numerical results

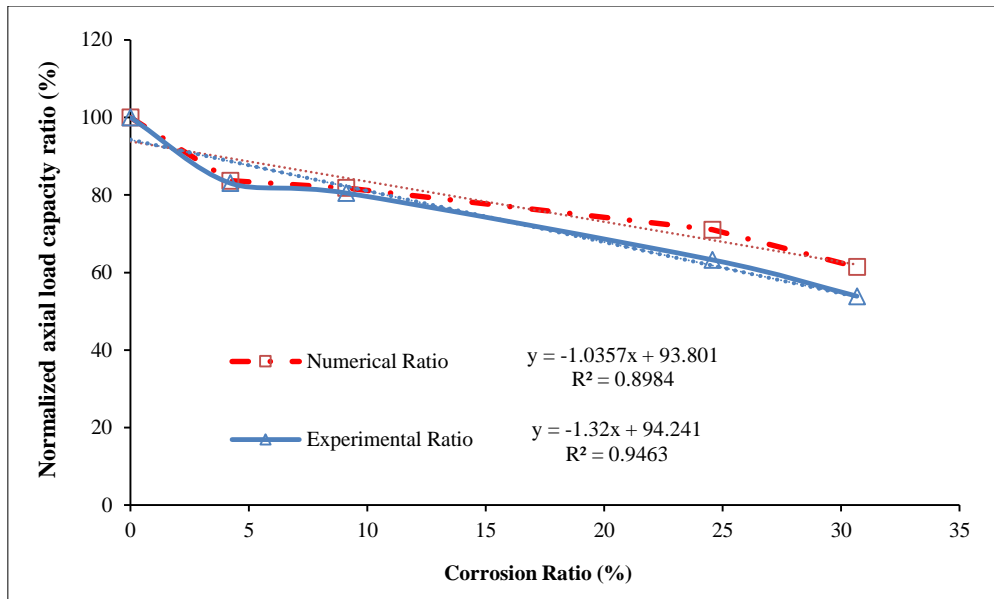|	Experimental result			Numerical result			(Num/Exp.) Ratio	
	Displacement (mm)	Load (kN)	Axial load capacity ratio (%)	Displacement (mm)	Load (kN)	Axial load capacity ratio (%)	Disp.	Load
Sp 0	7.86	42.6	100	7.38	40.2	100	0.93	0.94
Sp 4.21	7.67	35.4	83	7.22	33.6	83.5	0.94	0.95
Sp 9.11	6.61	34.3	80.5	6.76	32.9	81.8	1.02	0.96
Sp 24.56	6.64	26.9	63	6.73	28.6	71	1.01	1.06
Sp 30.67	7.25	22.9	53.7	5.95	24.7	61.4	0.82	1.07

Figure 17. Corrosion ratio (%) and axial load capacity (%)

5. Numerical Results and Discussion of Prototype-Scale Model

The numerical simulation results for corrosion explain the degradation of axial loading performance in reinforced concrete (RC) isolated footings on a prototype scale, with varying corrosion levels and concrete depths. The samples were of varying thicknesses, measuring 300 mm, 400 mm, and 500 mm, all with dimensions of 2000×2000 mm. Additionally, they had a clear cover thickness of 50 mm. The column involved using a steel tube that had dimensions of 300×300 mm, a 1000 mm height, and a thickness of 2 mm. The tube was then filled with reinforced concrete that had a compressive strength of 40 MPa. Thirteen steel bars with a diameter of 12 mm were utilized as longitudinal reinforcing steel in each direction. Tensile tests were carried out on the steel reinforcement, revealing a yield strength f_y of 500 MPa for the 12 mm-diameter bars.

5.1. Load – Deflection Curve of Prototype Scale 2000×2000×300 mm

Figures 18 and 19 display the curves that represent how the axial load and displacement are related for various prototype-scale models with an RC depth of 300 mm. The results of numerical analysis for prototype-scale corroded footings subjected to axial load indicate a significant decrease in both stiffness and ultimate loading bearing capacity compared to the control footing. Table 6 provides the values for failure load, displacement, and the ratio between the numerical and experimental results. The reduction ratio for the corroded footings relative to the control footing was 95.74%, 92.48%, 71.2%, and 65.1% for Sp4.21, Sp 9.11, Sp 24.56, and Sp 30.67, respectively.
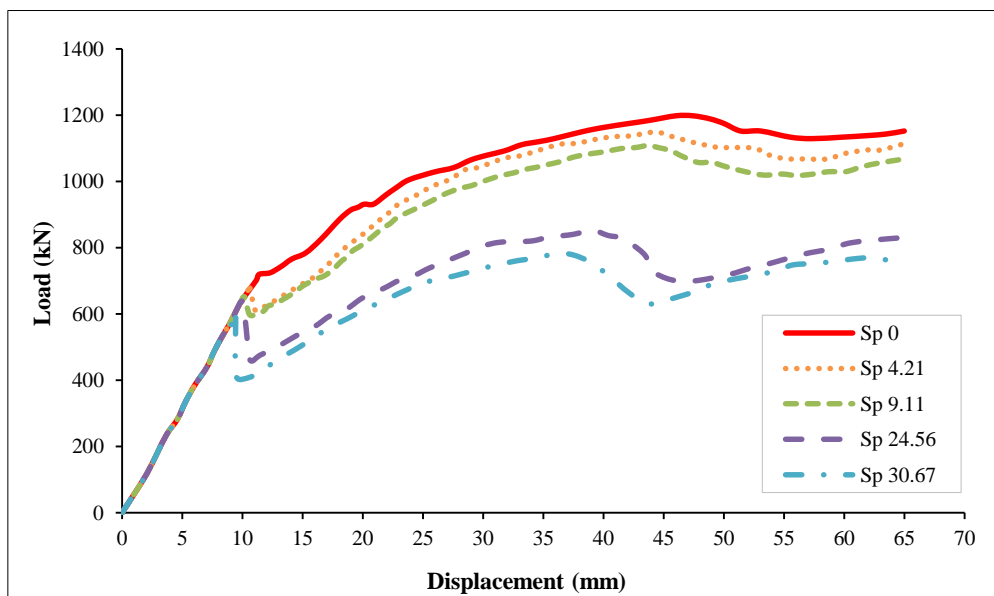

Figure 18. Numerical Envelope curve of the prototype-scale specimens; t=300 mm
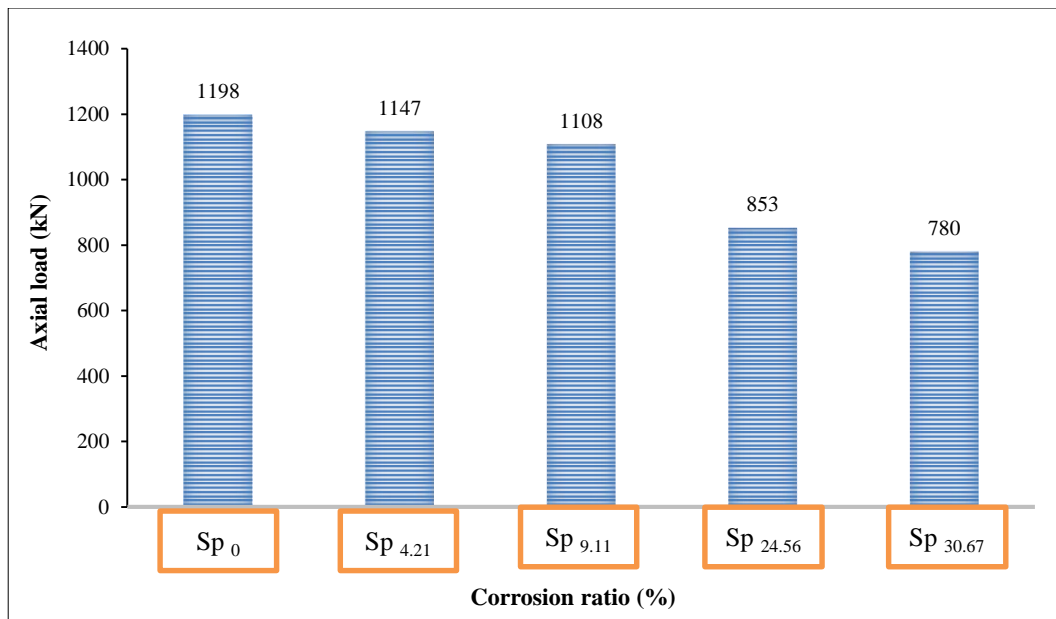
Figure 19. Comparison of load capacity; t=300 mm

Table 6. Numerical result for prototype scale footing 2000×2000×300 mm

	Prototype scale footing 2000×2000×300 mm		
	Load (kN)	Displacement (mm)	Axial load capacity ratio (%)
Sp 0	1198	46.02	100
Sp 4.21	1147	43.65	95.74
Sp 9.11	1108	43.74	92.48
Sp 24.56	853	39.02	71.2
Sp 30.67	780	35.87	65.1

Figure 20 Illustrate the correlation between the percentage of corrosion and the decrease in the load bearing capacity as a ratio compared to the standard specimen.

$$y = -1.1766x + 101.04 \tag{3}$$

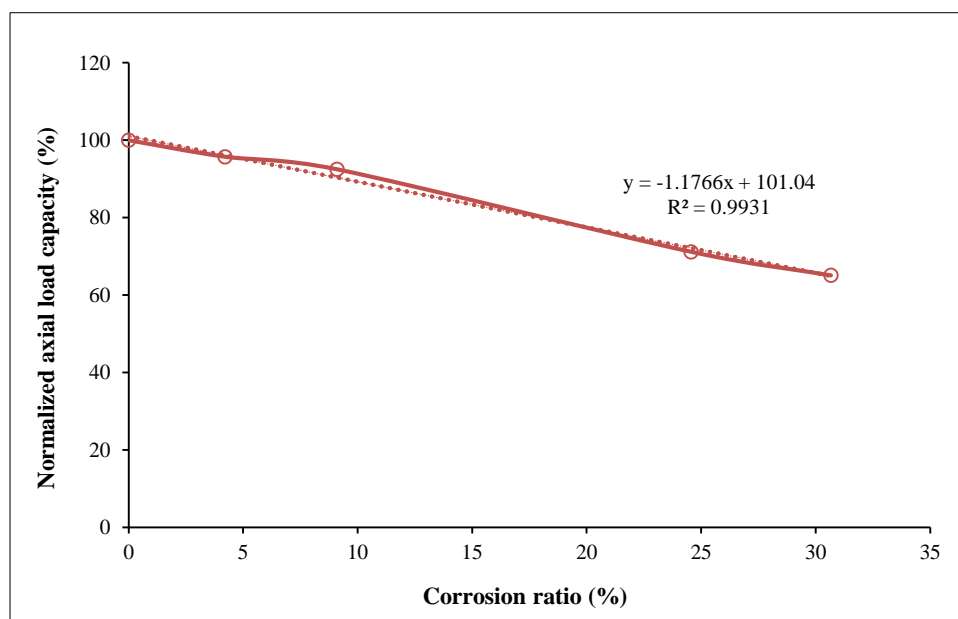where y is Normalized axial load capacity % and X is Corrosion ratio %.

Figure 20. Corrosion ratio (%) and axial load capacity (%); t=300 mm

5.2. Load–Deflection Curve of Large-Scale 2000×2000×400 mm

Figures 21 and 22 show the curves of the axial load-displacement responses of all specimens with a depth = 400 mm. The relationship between axial load capacity and displacement for prototype scale footings subjected to axial load is presented. The control footing shows a significant deterioration in both failure loads and stiffness. Table 7 displays the failure load, displacement, and ratio of numerical and experimental results. The reduction ratio for corroded footing concerning control footing was 94.6%, 92.6%, 74.8%, and 69.9% for Sp 4.21, Sp 9.11, Sp 24.56, and Sp 30.67, respectively.
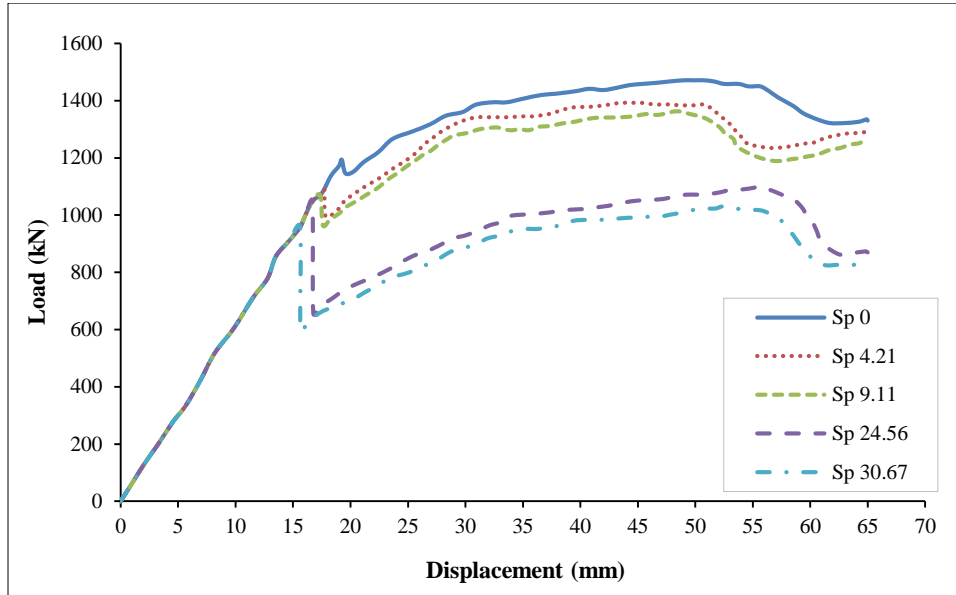

Figure 21. Numerical Envelope curve of the prototype-scale specimens; t=400 mm
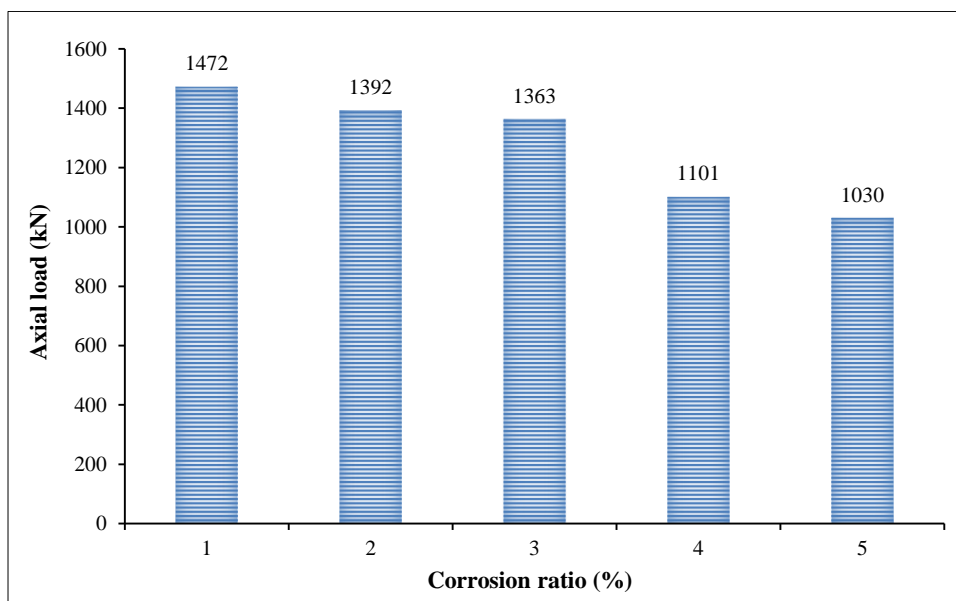
Figure 22. Comparison of load capacity; t=400 mm

Table 7. Numerical result for large-scale footing 2000×2000×400mm

	Prototype scale footing 2000×2000×400 mm		
	Load (kN)	Displacement (mm)	Axial load capacity ratio (%)
Sp 0	1472	50.7	100
Sp 4.21	1392	45.3	94.6
Sp 9.11	1363	48.7	92.6
Sp 24.56	1101	55.7	74.8
Sp 30.67	1030	52.4	69.9

Figure 23 indicate the relation between the reduction in load bearing capacity as a ratio from the control specimen and corrosion ratio %.

$$y = -0.9891x + 99.946 \tag{4}$$

where y is normalized axial load capacity % and X is corrosion ratio %.

Figure 23. Corrosion ratio (%) and axial load capacity (%); t=400 mm

5.3. Load – Deflection Curve of Prototype Scale 2000×2000×500 mm

The results indicate a significant degradation in stiffness and loading capacity compared to the control footing as shown in Figures 24 and 25. Table 8 illustrate the failure load, displacement, and the ratio between the numerical results for each specimen. The reduction in failure load compared to the control footing was 91.5%, 88.5%, 83.6%, and 79.2% for Sp 4.21, Sp 9.11, Sp 24.56, and Sp 30.67, respectively.

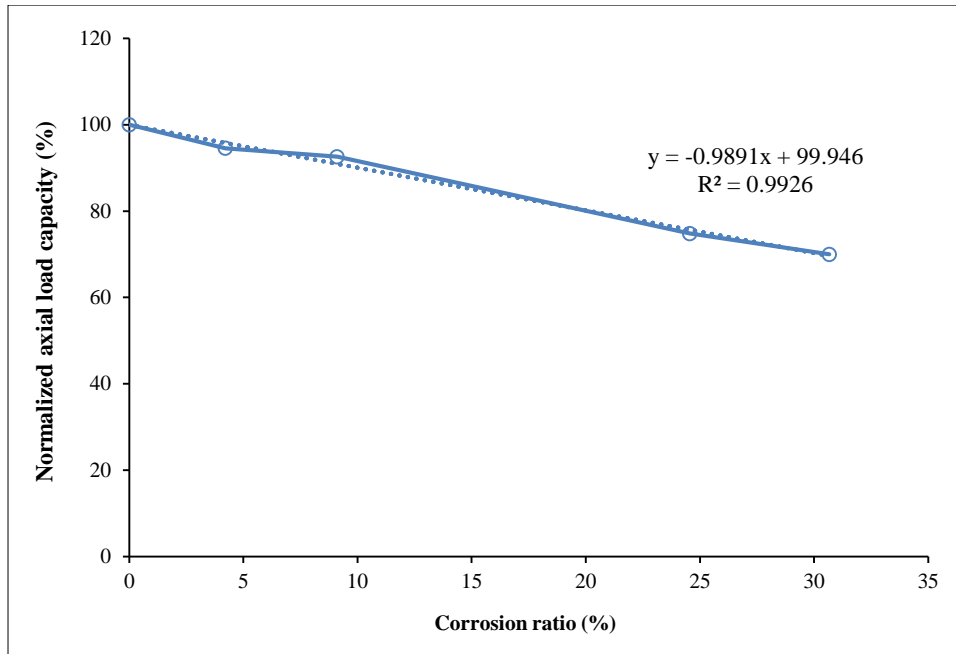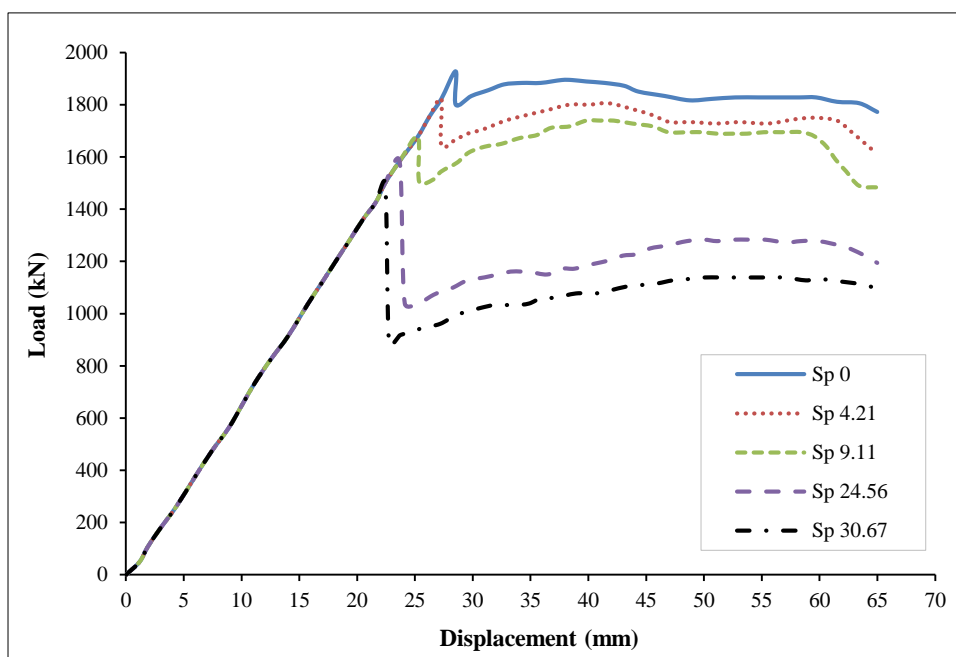**Figure 24. Numerical Envelope curve of the prototype scale specimens; t=500 mm**
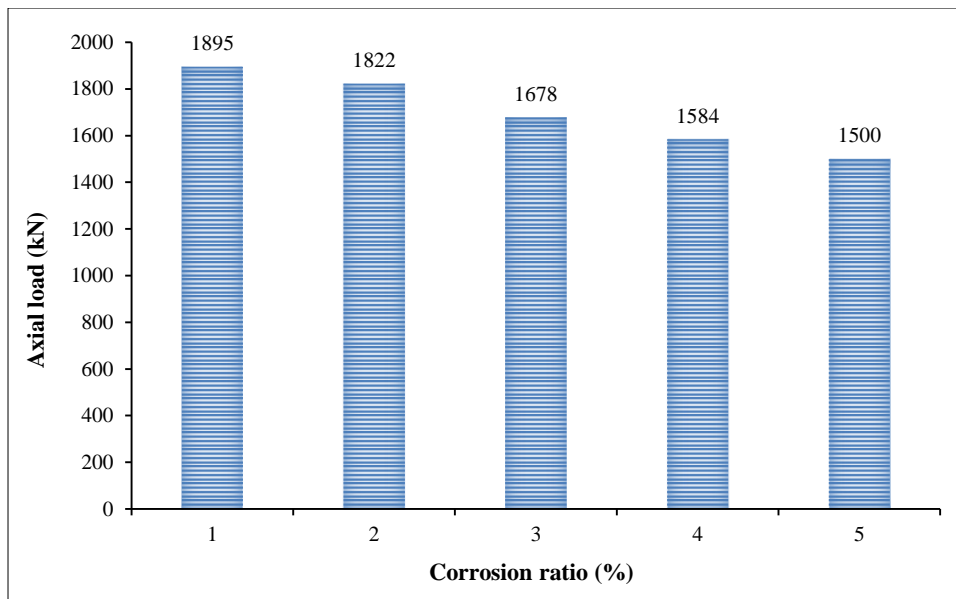
Figure 25. Comparison of load capacity; t=500 mm

Table 8. Numerical result for large-scale footing 2000×2000×500 mm

	Prototype scale footing 2000×2000×500 mm		
	Load (kN)	Displacement (mm)	Axial load capacity ratio (%)
Sp 0	1895	38.5	100
Sp 4.21	1822	27.3	96.1
Sp 9.11	1678	25.3	88.5
Sp 24.56	1584	23.7	83.6
Sp 30.67	1500	22.4	79.2

Figure 26 represent the relation between corrosion ratio % and the reduction in load bearing capacity as a ratio from the control specimen.

$$y = -0.6278x + 98.093 \tag{5}$$

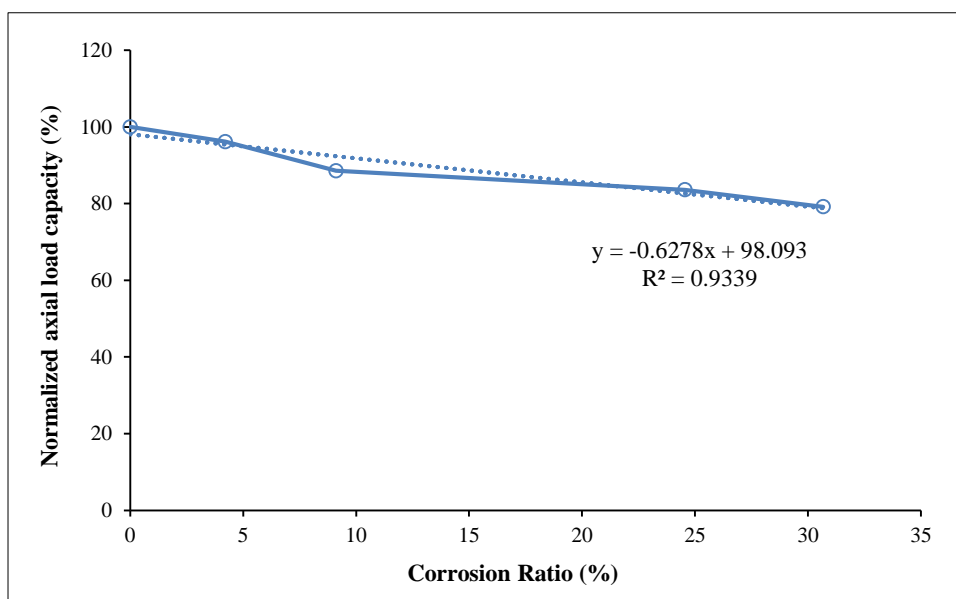where y is normalized axial load capacity % and X is corrosion ratio %.

Figure 26. Corrosion ratio (%) and axial load capacity (%); t=500 mm

5.4. Numerical Result for Large-Scale Footing with Different Depths

Table 9 illustrates the values of failure load, displacement, and the ratio between the numerical and experimental results for the prototype-scale samples. In Figure 27, the relation between the corrosion ratio (%) and axial load capacity is shown for all the prototype-scale footings with different concrete depths. It is noted that the results of the reduction in ultimate load for different corrosion ratios are similar when comparing the different concrete depths.

Table 9. Numerical result for prototype scale footing with different depths

			Displacement (mm)	Load (kN)	Axial load capacity (%)
Prototype-scale	Numerical results 2000×2000×300 mm Scale (1)	Sp 0	46.02	1198	100
		Sp 4.21	43.65	1147	95.74
		Sp 9.11	43.74	1108	92.48
		Sp 24.56	39.02	853	71.2
		Sp 30.67	35.87	780	65.1
	Numerical results 2000×2000×400 mm	Sp 0	50.7	1472	100
		Sp 4.21	45.3	1392	94.6
		Sp 9.11	48.7	1363	92.6
		Sp 24.56	55.7	1101	74.8
		Sp 30.67	52.4	1030	69.9
	Numerical results 2000×2000×500 mm	Sp 0	38.5	1895	100
		Sp 4.21	27.3	1822	96.1
		Sp 9.11	25.3	1678	88.5
		Sp 24.56	23.7	1584	83.6
		Sp 30.67	22.4	1500	79.2

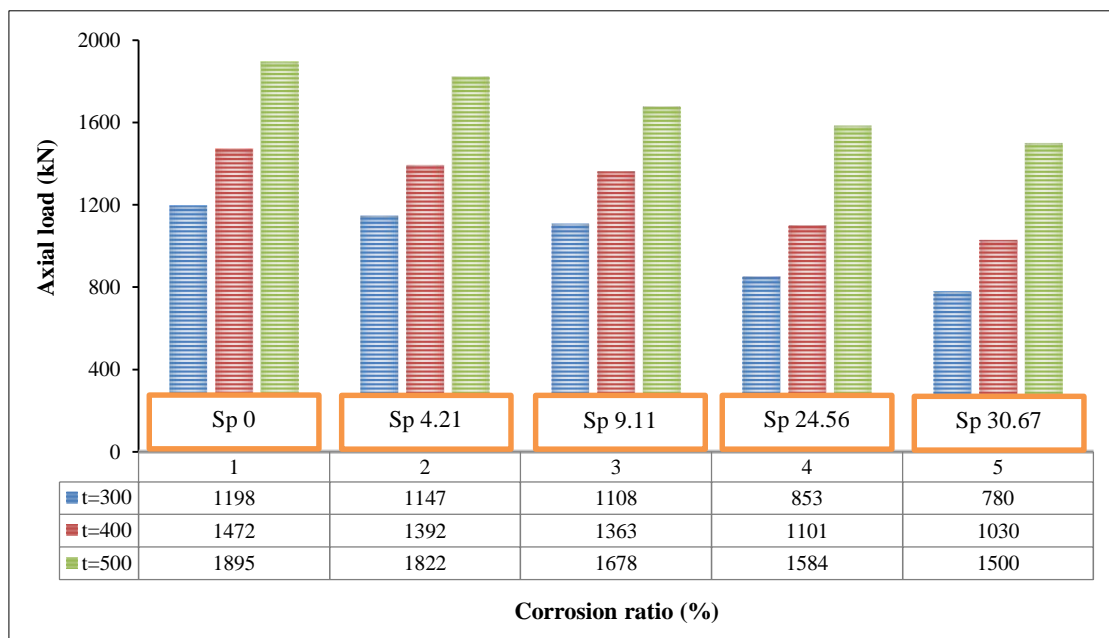|	Sp 0	Sp 4.21	Sp 9.11	Sp 24.56	Sp 30.67
	1	2	3	4	5
t=300	1198	1147	1108	853	780
t=400	1472	1392	1363	1101	1030
t=500	1895	1822	1678	1584	1500

Figure 27. Represent the relation between corrosion ratio % and axial load capacity for all the prototype-scale footing with different (RC) depths

Figures 28 and 29 represent the correlation between the corrosion ratio percentage and the reduction in axial load capacity as a ratio from the control specimen for small and prototype-scale footings, respectively.

$$y = -0.6278x + 98.093 \tag{6}$$

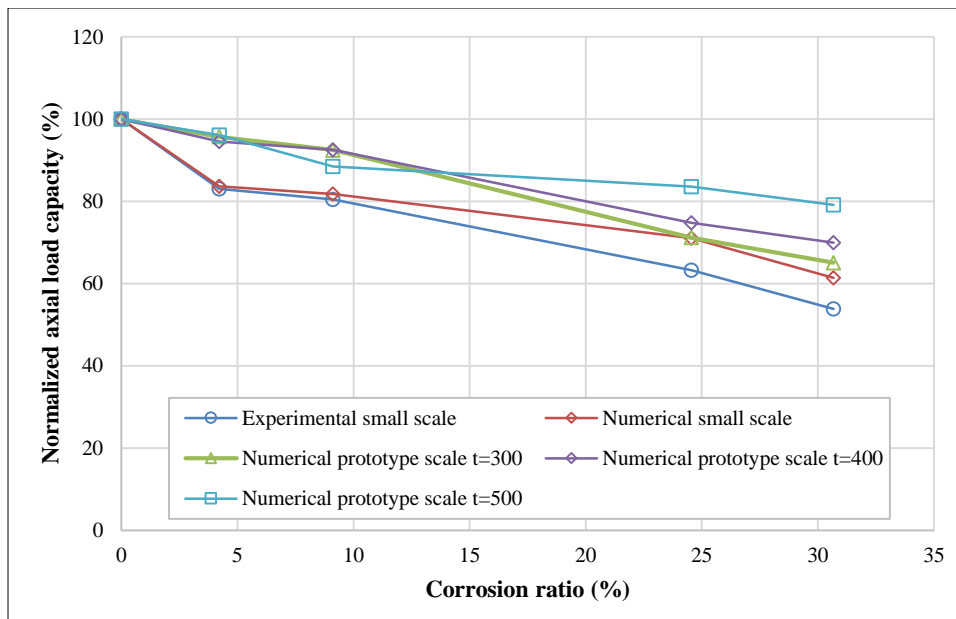where y is normalized axial load capacity % and X is corrosion ratio %.

Figure 28. Corrosion ratio % and axial load capacity % for small-and-prototype-scale footing
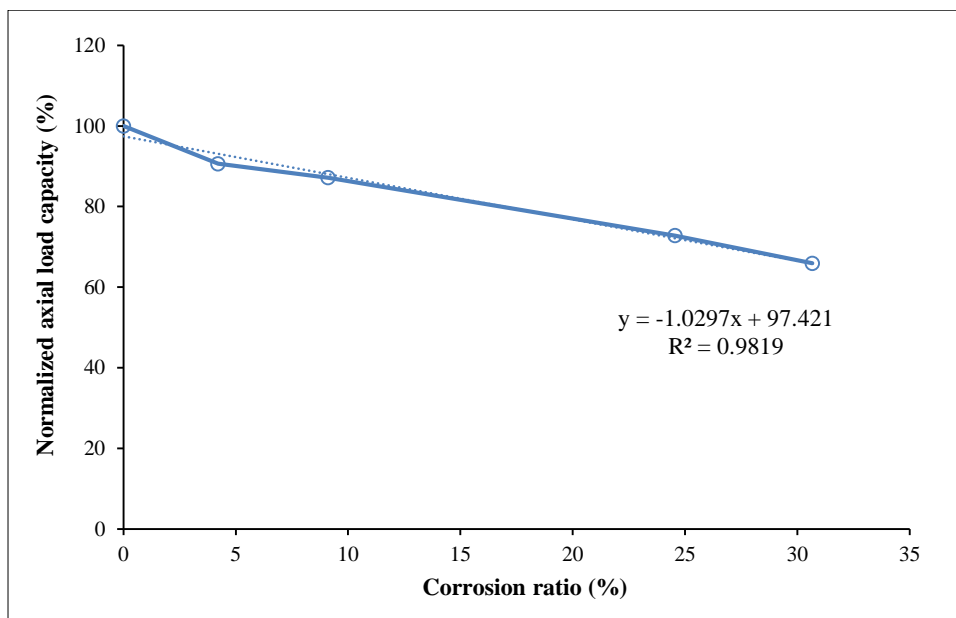

Figure 29. Axial load capacity % and Corrosion ratio % and for small-and-prototype-scale footing as the average ratio

With increasing corrosion ratios, the normalized axial load capacity of reinforced concrete footings decreases for both small and prototype-scale footings. The negative slope of the equation (-1.0297) shows that the reduction in the capacity load is more significant for higher corrosion ratios. The y-intercept of 97.421 represents the normalized axial load capacity when the corrosion ratio is 0%. Overall, this analysis indicates that corrosion has a substantial impact on the axial load capacity of reinforced concrete footings, with higher corrosion ratios resulting in greater reductions in load-bearing capacity.

6. Code Specification for Calculating the Ultimate Load of Isolating Footing

Concerning the ECP 203, Egyptian code [19] for calculating the ultimate load for isolated footing. The ultimate load is the smallest value from the ultimate flexure load and the punching load to ensure that the footing is safe in flexure failure and punching failure.

- *Calculating the flexure ultimate load capacity*

$$T = C \tag{7}$$

$$As \times \frac{fy}{\gamma s} = 0.67 \times \frac{fcu}{\gamma c} \times b \times a \tag{8}$$

Get a=…

$$C_b = (\frac{600}{600 + \frac{fy}{\gamma s}}) \times d \tag{9}$$

$$a_b = 0.8 \times C_b \tag{10}$$

Get a_b=…

$$a < a_b \tag{11}$$

$$M_u = C \times (d - \frac{a}{2}) = (0.67 \times \frac{fcu}{\gamma c} \times b \times a) \times (d - \frac{a}{2}) \tag{12}$$

$$M_u = q_{su} \times \frac{(Ar - ac)^2}{8} \tag{13}$$

$$q_{su} = \frac{Pu}{Ar \times Br} \tag{14}$$

get (p_u) = …..

where T is tension force in steel bar, C is compression force in stress block, F_y is yield stress, F_{cu} is compression stress of concrete, C_b is compression distance in balance state, d is concrete depth, M_u is ultimate moment resistance, q_{su} is ultimate punching strength, γc is reduction factor for concrete is 1.5, γs is reduction factor for steel is 1.15, $Ar * Br$ is punching area.

- *Calculating the punching ultimate load capacity*

$$q_{su} = \frac{Pu}{Ar \times Br} = \frac{1.4 \times PD.L + 1.6 \times PL.L}{Ar \times Br} \tag{15}$$

$$(b_o) = 2 \times (a \times b) = 2(a_c + d) + 2(b_c + d) \tag{16}$$

$$Q_{up} = P_u - q_{su} (a \times b) \tag{17}$$

$$q_{up} = \frac{Q_{up}}{bo * d} \leq q_{cup} \tag{18}$$

since punching shear q_{up} should be less than concrete strength q_{cup} by the ECP203, the developed shear is given by the least of the following three values:

$$q_{cup} = 0.316 \sqrt{\frac{Fcu}{\gamma c}} \leq 1.6 \text{ N/mm}^2 \tag{19}$$

$$q_{cup} = 0.316 (0.50 + \frac{a}{b}) \sqrt{\frac{Fcu}{\gamma c}} \tag{20}$$

$$q_{cup} = 0.8 (0.20 + \frac{\alpha d}{bo}) \sqrt{\frac{Fcu}{\gamma c}} \tag{21}$$

where α is a factor for corner, exterior, internal footing equal to 2,3,4, respectively and b_o is the perimeter for punching shear.

The failure loads of non-corroded footing with different depths were compared with the ECP203 (Egyptian Code, 2018) provision and how corrosion ratios can be calculated by numerical models. It was found that the variation between the design loads and numerical loads for controlled footing with thicknesses of 300, 400, and 500 mm was (73%, 80%, and 78%), respectively. It's induced that the equivalent corrosion ratios% by using the deduced relation were (23.8%, 20.2%, and 32%), respectively, as shown in Table 10.

Table 10. Comparison between the design load and numerical load

	Pu (kN) Numerical	Pu (ECP203) code			(Design. Load /Numerical load) ratio (%)	Equivalent corrosion ratio (%)
		Pu (kN) Flexure load	Pu (kN) Punching Load	Pu (kN) Design load		
T=300	1198	875.54	1404.87	875.54	73 %	23.8%
T=400	1472	1176.28	2488.88	1176.28	80 %	20.2%
T=500	1895	1477.17	4266.67	1477.17	78 %	32%

7. Conclusions

In conclusion, the study has shown that:

- The steel expansion model that accounts for corrosion is a dependable technique for simulating the corrosion damage in isolated reinforced concrete footings;

- The stiffness of the finite element model used to predict the elastic behavior of the reinforced concrete isolated footing was larger than that of the experimental footing;

- At a same depth, the decrease in ultimate load amplifies as the level of corrosion becomes more severe;

- The mean alteration of ultimate load, as determined by both experimentation and finite element modeling, was discovered to be below 5.6% for small-scale testing, while the average variance in deflection was 6.8%;

- The cracking pattern showed that cracks began as flexure cracks and progressed to punching as the corrosion rate increased;

- There were some differences in the appearance of cracks in the samples subjected to high levels of corrosion due to the uniform representation of rust in the rebar in the ABAQUS software;

- The variation between the design loads by code and the numerical loads by ABAQUS for controlled footings with thicknesses of 300, 400, and 500 mm was found to be 73, 80, and 78%, respectively;

- By using the deduced relationship, the equivalent corrosion ratio percentages were 23.8, 20.2, and 32%, respectively.

The conclusion of the study suggests that the findings can have significant implications for building codes and standards, as they can be used to update the assessment and mitigation provisions for the effects of corrosion on reinforced concrete isolated footings. This will help ensure the long-term safety and reliability of structures. The results of the study can also contribute to the development of more resilient and sustainable infrastructure by enhancing our comprehension of how corrosion impacts the performance of RC isolated footings.

However, it's important to note that while the steel expansion model for corroded steel is a valuable method for modeling the behavior of corroded reinforced concrete footings, it has its limitations. As a result, it should be used in combination with other procedures and approaches to assure the results' correctness and dependability.

8. Declarations

8.1. Author Contributions

8.2. Data Availability Statement

The data presented in this study are available in the article.

8.3. Funding

8.4. Conflicts of Interest

The authors declare no conflict of interest.

9. References

[1] Yan, X., & Yu, H. (2022). Numerical simulation of hydraulic fracturing with consideration of the pore pressure distribution based on the unified pipe-interface element model. Engineering Fracture Mechanics, 275. doi:10.1016/j.engfracmech.2022.108836.

[2] Ye, H., Fu, C., Tian, Y., & Jin, N. (2020). Chloride-induced steel corrosion in concrete under service loads. Springer, Singapore. doi:10.1007/978-981-15-4108-7.

[3] Shang, Z., Zheng, S., Zheng, H., Li, Y. L., & Dong, J. (2022). Seismic behavior and damage evolution of corroded RC columns designed for bending failure in an artificial climate. Structures, 38, 184–201. doi:10.1016/j.istruc.2022.01.072.

[4] Ma, Y., Che, Y., & Gong, J. (2012). Behavior of corrosion damaged circular reinforced concrete columns under cyclic loading. Construction and Building Materials, 29, 548–556. doi:10.1016/j.conbuildmat.2011.11.002.

[5] Zaghian, S., Martín-Pérez, B., & Almansour, H. (2023). Finite element modelling of bridge piers subjected to eccentric load combined with reinforcement corrosion. Engineering Structures, 283, 0141–0296. doi:10.1016/j.engstruct.2023.115822.

[6] El-Joukhadar, N., Dameh, F., & Pantazopoulou, S. (2023). Seismic Modelling of Corroded Reinforced Concrete Columns. Engineering Structures, 275, 0141–0296. doi:10.1016/j.engstruct.2022.115251.

[7] Wang, Y., Wang, W., Huang, J., & Luo, L. (2023). Effect of corrosion on soil-structure interfacial shearing property and bearing capacity of steel foundation in submarine soil environment. Computers and Geotechnics, 156, 0266–352. doi:10.1016/j.compgeo.2023.105269.

[8] Wang, W., Wang, Y., Huang, J., & Luo, L. (2022). Surface roughness characteristics and stochastic model of corroded steel foundation in submarine soil environment. Ocean Engineering, 251, 0029–8018. doi:10.1016/j.oceaneng.2022.111177.

[9] Li, M., Shen, D., Yang, Q., Cao, X., Huang, C., Cui, Z., & Qi, Y. (2023). Effect of reinforcement corrosion on the seismic performance of reinforced concrete shear walls. Construction and Building Materials, 377, 0950–0618. doi:10.1016/j.conbuildmat.2023.130977.

[10] Han, X., Wang, P., Cui, D., Tawfik, T. A., Chen, Z., Tian, L., & Gao, Y. (2023). Rebar corrosion detection in concrete based on capacitance principle. Measurement, 209, 112526. doi:10.1016/j.measurement.2023.112526.

[11] Zheng, Y., Zheng, S. S., Yang, L., Dong, L. G., Ruan, S., & Ming, M. (2022). Experimental study on the seismic behavior of corroded reinforced concrete walls in an artificial climate corrosion environment. Engineering Structures, 252, 0141–0296. doi:10.1016/j.engstruct.2021.113469.

[12] Zhao, J., Lin, Y., Li, X., & Meng, Q. (2021). Experimental study on the cyclic behavior of reinforced concrete bridge piers with non-uniform corrosion. Structures, 33, 999–1006. doi:10.1016/j.istruc.2021.04.060.

[13] Hu, Z., Hua, L., Liu, J., Min, S., Li, C., & Wu, F. (2021). Numerical simulation and experimental verification of random pitting corrosion characteristics. Ocean Engineering, 240, 0029–8018. doi:10.1016/j.oceaneng.2021.110000.

[14] Altoubat, S., Maalej, M., & Shaikh, F. U. A. (2016). Laboratory Simulation of Corrosion Damage in Reinforced Concrete. International Journal of Concrete Structures and Materials, 10(3), 383–391. doi:10.1007/s40069-016-0138-7.

[15] Kashani, M. M., Lowes, L. N., Crewe, A. J., & Alexander, N. A. (2016). Computational modelling strategies for nonlinear response prediction of corroded circular RC bridge piers. Advances in Materials Science and Engineering, 2016, 15. doi:10.1155/2016/2738265.

[16] Mohammed, A. M. Y., Ahmed, A., & Maekawa, K. (2020). Comparative Nonlinear Behavior of Corroded Circular and Square RC Columns. KSCE Journal of Civil Engineering, 24(7), 2110–2119. doi:10.1007/s12205-020-1730-6.

[17] Khalid, N. (2018). Strength Reduction of Reinforced Concrete Columns Subjected to Corrosion Related Cover Spalling. Ph.D. Thesis, University of Akron, Columbus, United States.

[18] Fang, L., Zhou, Y., Yi, D., & Yi, W. (2021). Experimental study on flexural capacity of corroded RC slabs reinforced with basalt fiber textile. Applied Sciences (Switzerland), 11(1), 1–25. doi:10.3390/app11010144.

[19] E203-2018. (2018). Egyptian code for design and construction of reinforced concrete structures. Egyptian Code of Practice, Utilities and Urban Communities, Ministry of Housing, Cairo, Egypt.

[20] Li, Q., Jin, X., Yan, D., Fu, C., & Xu, J. (2021). Study of wiring method on accelerated corrosion of steel bars in concrete. Construction and Building Materials, 269, 121286. doi:10.1016/j.conbuildmat.2020.121286.

[21] Van Steen, C., Verstrynge, E., Wevers, M., & Vandewalle, L. (2019). Assessing the bond behaviour of corroded smooth and ribbed rebars with acoustic emission monitoring. Cement and Concrete Research, 120, 176–186. doi:10.1016/j.cemconres.2019.03.023.

[22] Abaqus 6.14. (2014). Abaqus 6.14 analysis user's Guide. Abaqus Inc., Johnston, United States. Available online: https://www.3ds.com/products-services/simulia/ (accessed on April 2023).

[23] Taqi, F. Y., Mashrei, M. A., & Oleiwi, H. M. (2021). Numerical Analysis of Corrosion Reinforcements in Fibrous Concrete Beams. Civil and Environmental Engineering, 17(1), 259–269. doi:10.2478/cee-2021-0027.

[24] German, M., & Pamin, J. (2015). FEM simulations of cracking in RC beams due to corrosion progress. Archives of Civil and Mechanical Engineering, 15(4), 1160–1172. doi:10.1016/j.acme.2014.12.010.